Supplementary Note 1. Rational design and molecular evolution of red-shifted miRFP718nano.

In miRFP670nano, the biliverdin (BV) chromophore forms a covalent thioether bond between the $C3^1$ atom of ring A of BV and Cys86 residue conserved in CBCRs[1] (**Supplementary Fig. 1a,b**). The formation of this covalent bond leads to the reduction of ring A, shortening the chromophore conjugated system, and, hence, a hypsochromic shift of its fluorescence. Instead, in wild-type BphPs and many BphP-derived red-shifted FPs, BV is attached to the protein by the $C3^2$ atom of ring A, and ring A remains oxidized[2]. The structure of miRFP670nano[1] revealed that C^{β} and C^{γ} atoms of Arg57 are positioned close to the $C3^2$ atom. We hypothesized that substitutions Arg57Cys and Cys86Ser could enable a covalent binding of BV via the $C3^2$ atom, resulting in a red shift. To evaluate this, we engineered miRFP670nano/Arg57Cys/Cys86Ser double-mutant. The mutant had fluorescence spectra 35 nm red-shifted as compared to parental miRFP670nano (**Supplementary Fig. 1c**). To find the brightest mutant, position at 86 was subjected to saturated mutagenesis (**Supplementary Fig. 1d,e**). Expectedly, the clone containing Cys86 has double-peaked spectra, indicating chromophore heterogeneity (**Supplementary Fig. 1f**). Mutant containing Ser86 outperformed other clones in mammalian cells (**Supplementary Fig. 1e**).

To red-shift the spectra further, we performed saturated mutagenesis of miRFP670nano/Arg57Cys/Cys86Ser at residues 113-117 surrounding chromophore ring D, and found a more red-shifted mutant with two extra mutations Leu114Phe and Val115Ser (**Supplementary Fig. 1g**). To increase its brightness, we subjected it to random mutagenesis. The 14 rounds of molecular evolution resulted in NIR FP, named miRFP718nano, having 26 mutations relative to miRFP670nano (**Supplementary Fig. 2**).

Supplementary Note 2. Chromophore environment of miRFP718nano.

miRFP718nano differs from its progenitor miRFP670nano by twenty-six amino acid residues, seventeen of which are located on the surface, and nine are buried inside the protein.

miRFP718nano and miRFP670nano have similar but not identical chromophore environments (**Extended Data Fig. 1h,i**). In addition to eight hydrogen bonds and two stacking interactions common for both proteins, miRFP718nano has an extra H-bond between ring D of BV and Ser115 (Val115 in miRFP670nano) and the third tilted face-to-edge stacking between ring D and Phe90 (Leu90 in miRFP670nano). Val37Ile substitution in miRFP718nano alters the shape of the BV binding pocket, which becomes a better match to the chromophore size and shape compared to miRFP670nano. Val39Tyr substitution in miRFP718nano restrains the movement of the N-terminal α-helix by forming an H-bond with Asp5. The stabilizing hydrophobic cluster interconnecting N- and C-terminal α-helixes with the central β-sheet of the protein is reinforced by substitutions Thr11Ile, Val24Leu, and Leu114Phe. Large side chains of Leu24 and Phe114 fuse two previously separated hydrophobic clusters, one formed by residues Leu8, Ile11, Val12, Val26, Ile104, Leu114, Met140 and the other by Val15, Phe18, Leu19, Trp128, Phe132, Leu133 (**Extended Data Fig. 1l**). The interactions between β-strands two and three are further strengthened by hydrogen bonds between residues Glu30, Asn36, and His53 that contribute to the enhanced rigidity of a single GAF domain protein scaffold.

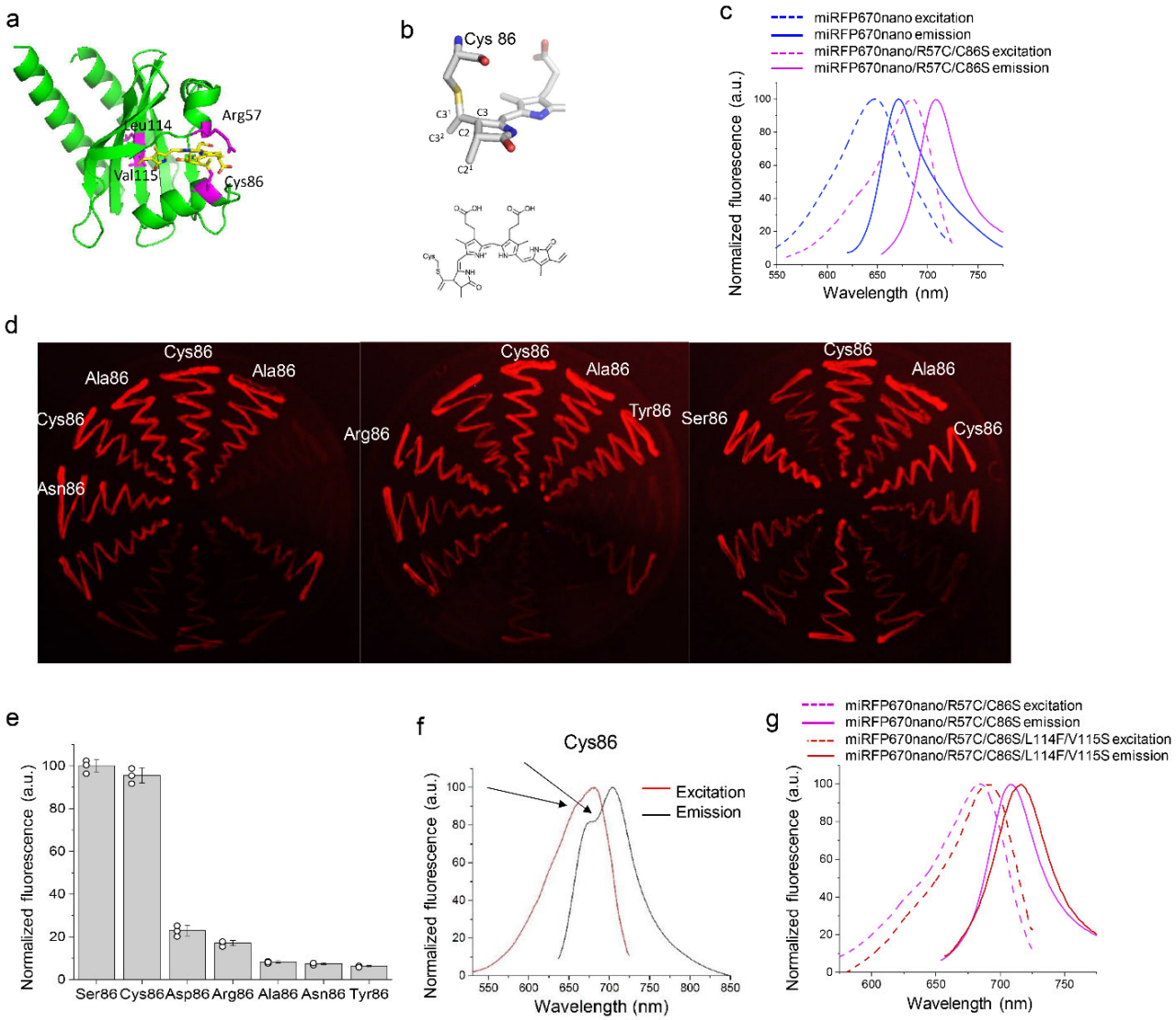

Supplementary Figure 1. Rational design of miRFP718nano. (a) miRFP670nano structure. Key residues responsible for the spectral shift are in magenta. **(b)** The chromophores in miRFP670nano bound to the Cys86 residue and its chemical formula. **(c)** Excitation and emission spectra of miRFP670nano and miRFP670nano/R57C/C86S mutant. **(d)** Saturation mutagenesis position at 86. Bacteria expressing mutants grown on a petri dish. **(e)** Saturation mutagenesis position at 86. Cellular brightness of the clones selected in bacteria. Fluorescence intensity was measured by flow cytometry using a 640 nm excitation laser and a 670 nm long-pass emission filter in transiently transfected HeLa cells 48 h after transfection. Data are presented as mean values ± s.d. for $n = 3$ transfection experiments. **(f)** Excitation and emission spectra of miRFP670nanoR57C/C86 mutant. **(g)** Excitation and emission spectra of miRFP670nanoR57C/C86S and miRFP670nanoR57C/C86S/L114F/V115S mutants. In (c, f, g) spectroscopic measurements were performed in phosphate-buffered saline (PBS). Emission spectra were measured using excitation at 580 nm for miRFP670nano and at 650 nm for mutants, excitation spectra were measured using emission at 740 nm.

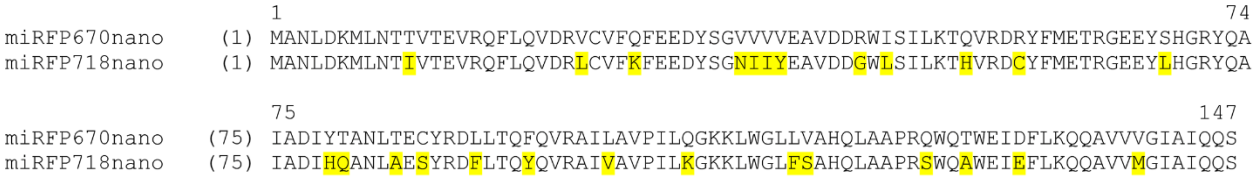

Supplementary Figure 2. Alignment of the amino acid sequences of miRFP670nano and miRFP718nano. Mutations found in miRFP718nano compared to miRFP670nano are highlighted in yellow.

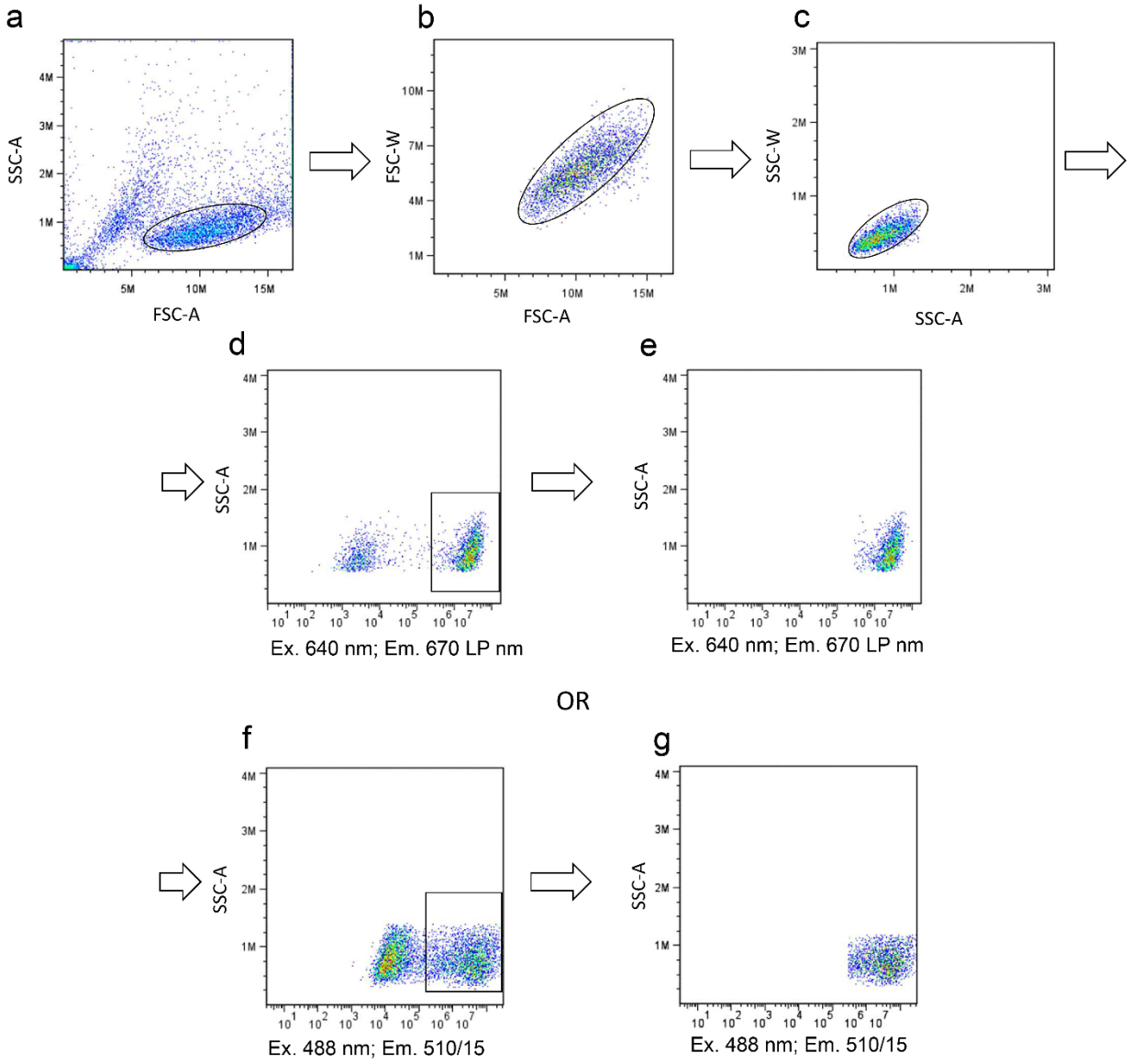

Supplementary Figure 3. Exemplifying gating strategy of FACS analysis. Gating was performed using three gates, for (**a**) intact cells, (**b**) single cells, and (**c**) live cells. These cells were then gated against untransfected cells in NIR (Ex. 640 nm, Em. 670 LP nm) channel for selecting NIR FPs positive cells (**d, e**), or in green (Ex. 488 nm, Em. 510/15 nm) channel for selecting EGFP positive cells (**f, g**).

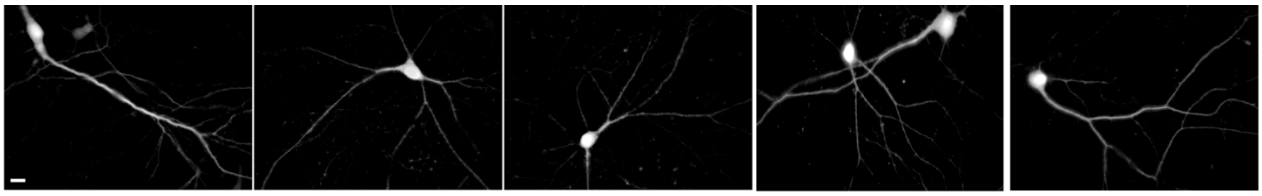

Supplementary Figure 4. miRFP718nano expressed in isolated primary cortical rat neurons. miRFP718nano's fluorescence is distributed evenly through neuron bodies and processes. Representative images of two experiments are shown. Scale bar, 10 μm.

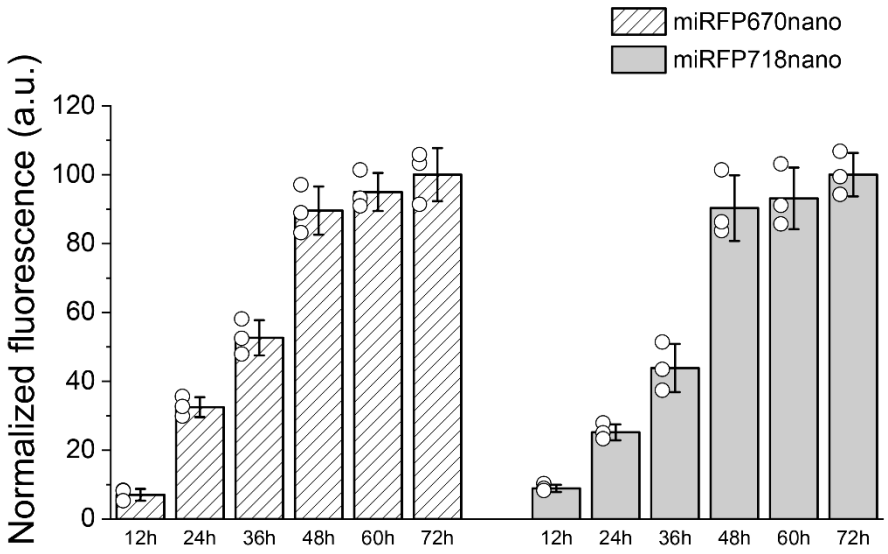

Supplementary Figure 5. Fluorescence intensity of HeLa cells transiently transfected with miRFP670nano and miRFP718nano measured at indicated time points after transfection. Data are presented as mean values ± s.d. for $n = 3$ transfection experiments. Fluorescence intensity was analyzed by flow cytometry using a 640 nm excitation laser and a 670 nm long-pass emission filter. Gating was performed as shown in Supplementary Fig. 3.

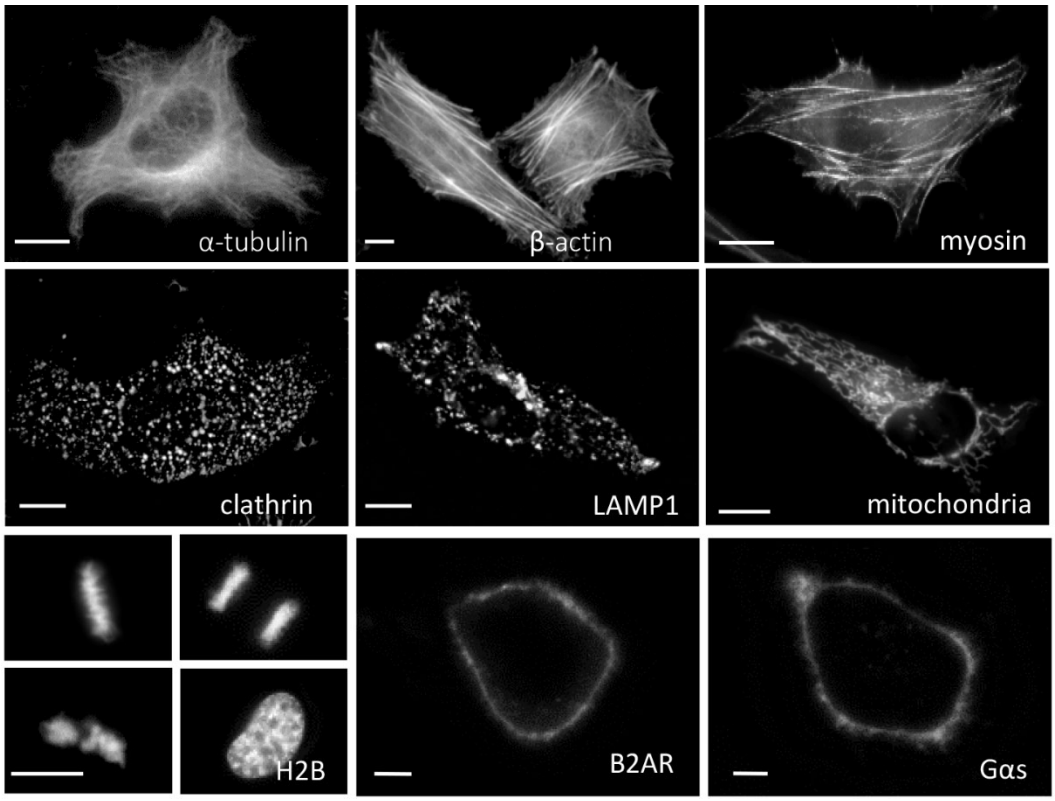

Supplementary Figure 6. miRFP718nano as protein fusions tag. Live HeLa cells transfected with the miRFP718nano N- terminal, C-terminal or internally inserted fusion constructs. The C-terminal fusions are α-tubulin, β-actin, myosin, and vesicular protein clathrin. The N-terminal fusions are lysosomal membrane glycoprotein LAMP1, mitochondria, and histone H2B. The internal fusions are β2 adrenergic receptor (β2AR) and G-protein α subunit (Gαs). Scale bars, 10 μm. Representative images of two experiments are shown.

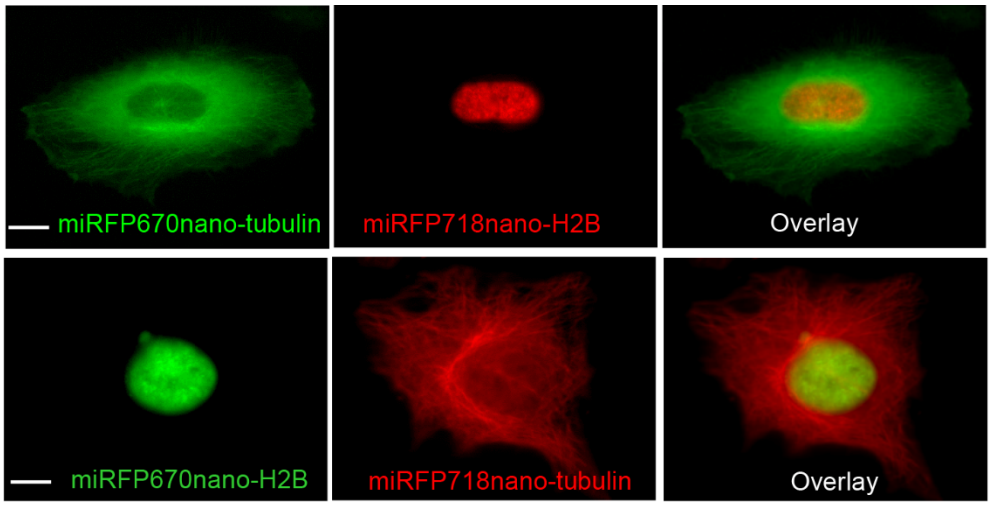

Supplementary Figure 7. Two-color images of cells co-expressing α-tubulin and H2B tagged with miRFP718nano or miRFP670nano, respectively. Scale bars, 10 μm. Representative images of two experiments are shown.

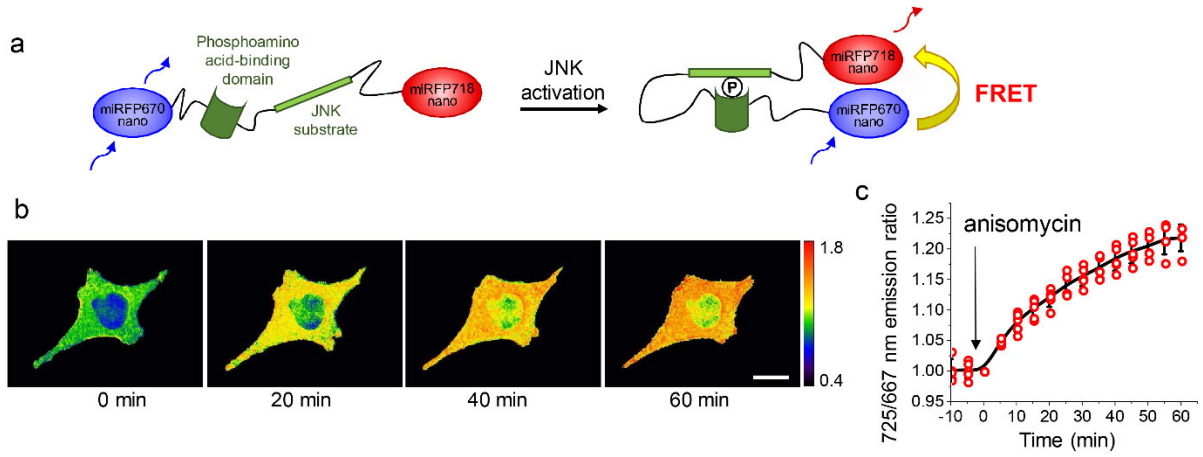

Supplementary Figure 8. NIR biosensors for detection of JNK kinase activity. (a) Schematic representation of miRFP670nano-miRFP718nano-based NIR FRET biosensor for JNK kinase activity. **(b)** Time-lapse 725/667 nm ratio images of HeLa cell expressing NIR JNK biosensor visualized using pseudocolor. Cells were stimulated with 1 μg/ml anisomycin. **(c)** The 725/667 nm ratio time-courses of HeLa cells expressing JNK biosensor stimulated with 1 μg/ml anisomycin. Data are presented as mean values ± s.d. for n = 4 transfection experiments. In (b, c) fluorescence signals were detected at 667 nm and 725 nm, respectively. Scale bars, 10 μm.

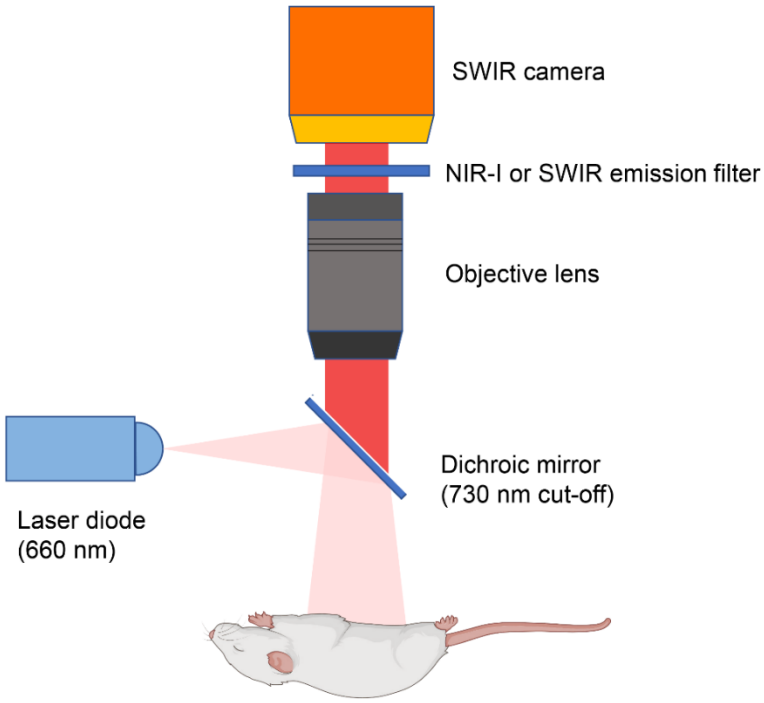

Supplementary Figure 9. Schematics of the lab-made NIR-I and SWIR imaging system. The NIR-I imaging and SWIR imaging share the same excitation source at 660 nm.

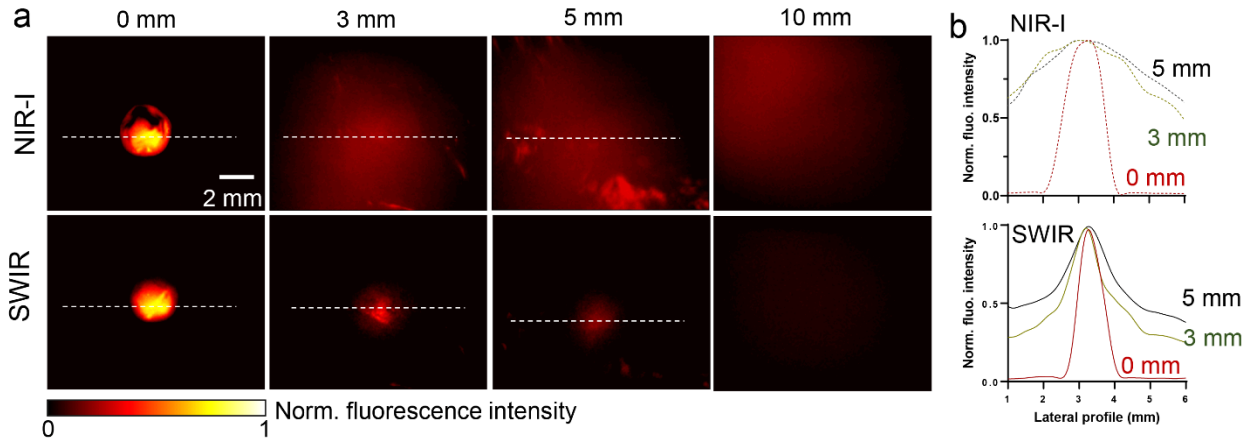

Supplementary Figure 10. NIR-I and SWIR imaging of miRFP718nano-expressing bacteria in phantom. (**a**) NIR-I and SWIR images of miRFP718nano-expressing bacteria drop overlayed by optically scattering medium at different depths from 0 mm to 10 mm. (**b**) The signal profiles of the bacteria drop along the dashed lines in (a) at 0 mm, 3 mm, and 5 mm depths in the NIR-I and SWIR images.

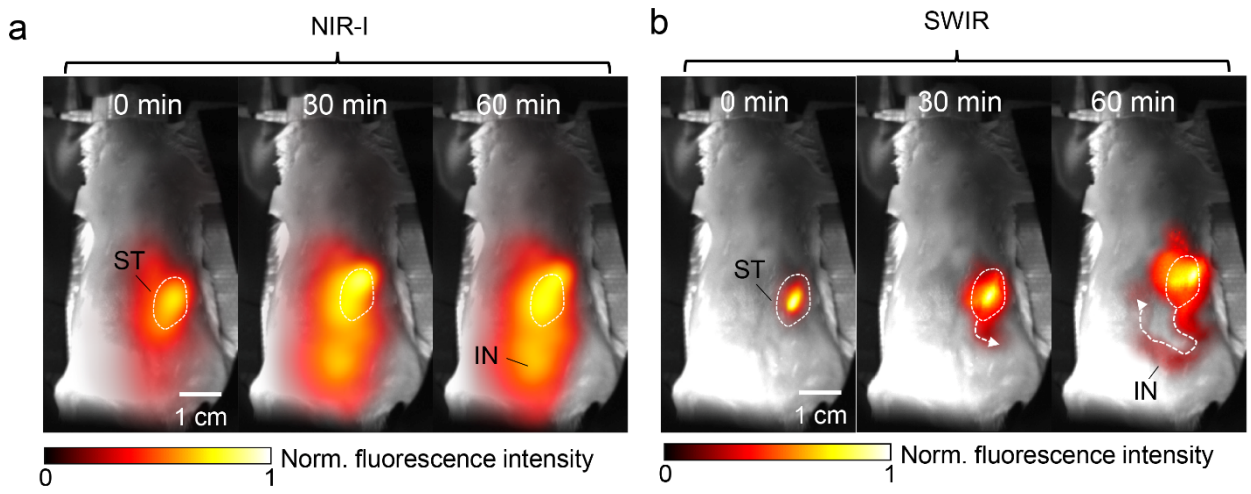

Supplementary Figure 11. NIR-I and SWIR imaging of bacteria movement in mouse digestion system. (**a**) The NIR-I images of the bacteria movement at different time points. ST, stomach; IN, intestine. (**b**) The corresponding SWIR images of the bacteria movement.

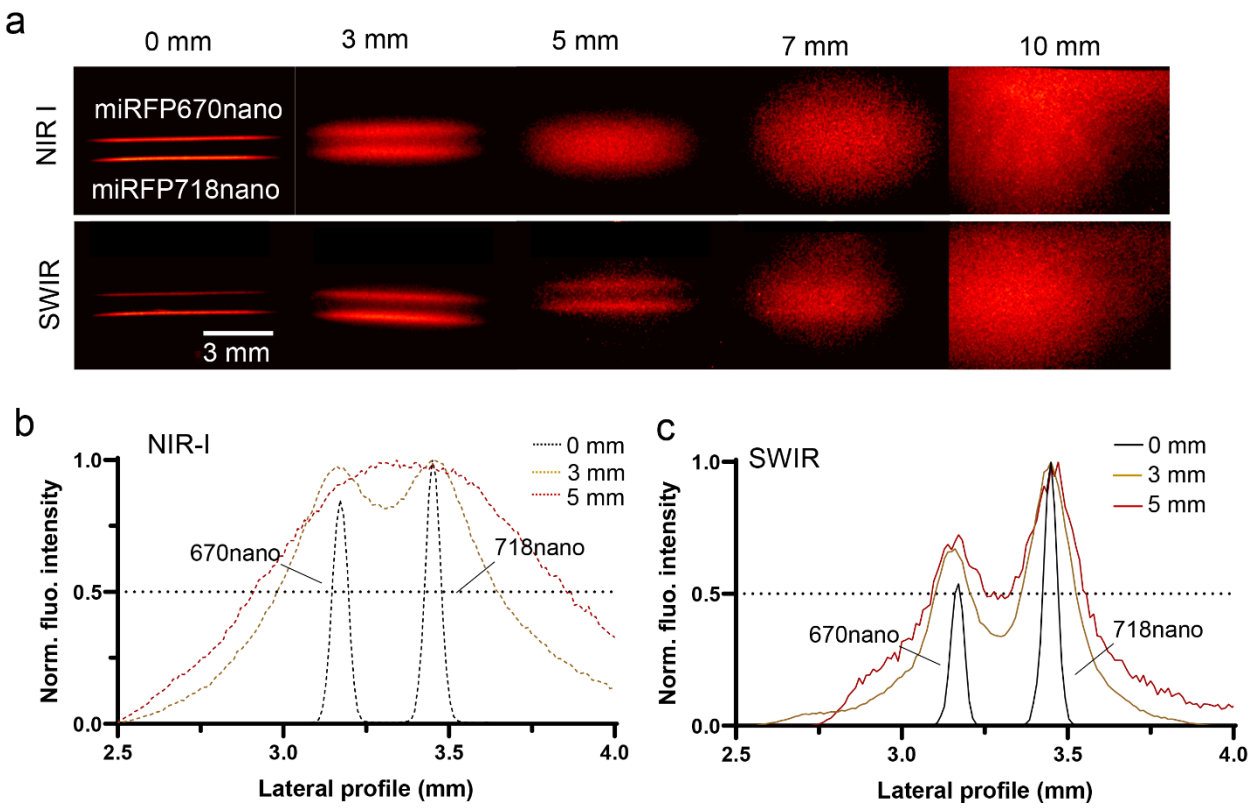

Supplementary Figure 12. NIR-I and SWIR imaging of miRFP718nano-expressing mammalian cells in phantom. (**a**) The NIR-I and SWIR images of a pair of 100-μm-diameter tubes filled with miRFP670nano- or miRFP718nano-expressing HEK293T cells, overlayed by optically scattering medium at depths up to 10 mm. (**b**) The NIR-I signal profiles across the pair of tubes at depth of 0 mm, 3 mm, and 5 mm. (**c**) The corresponding SWIR signal profiles at depth of 0 mm, 3 mm, and 5 mm.

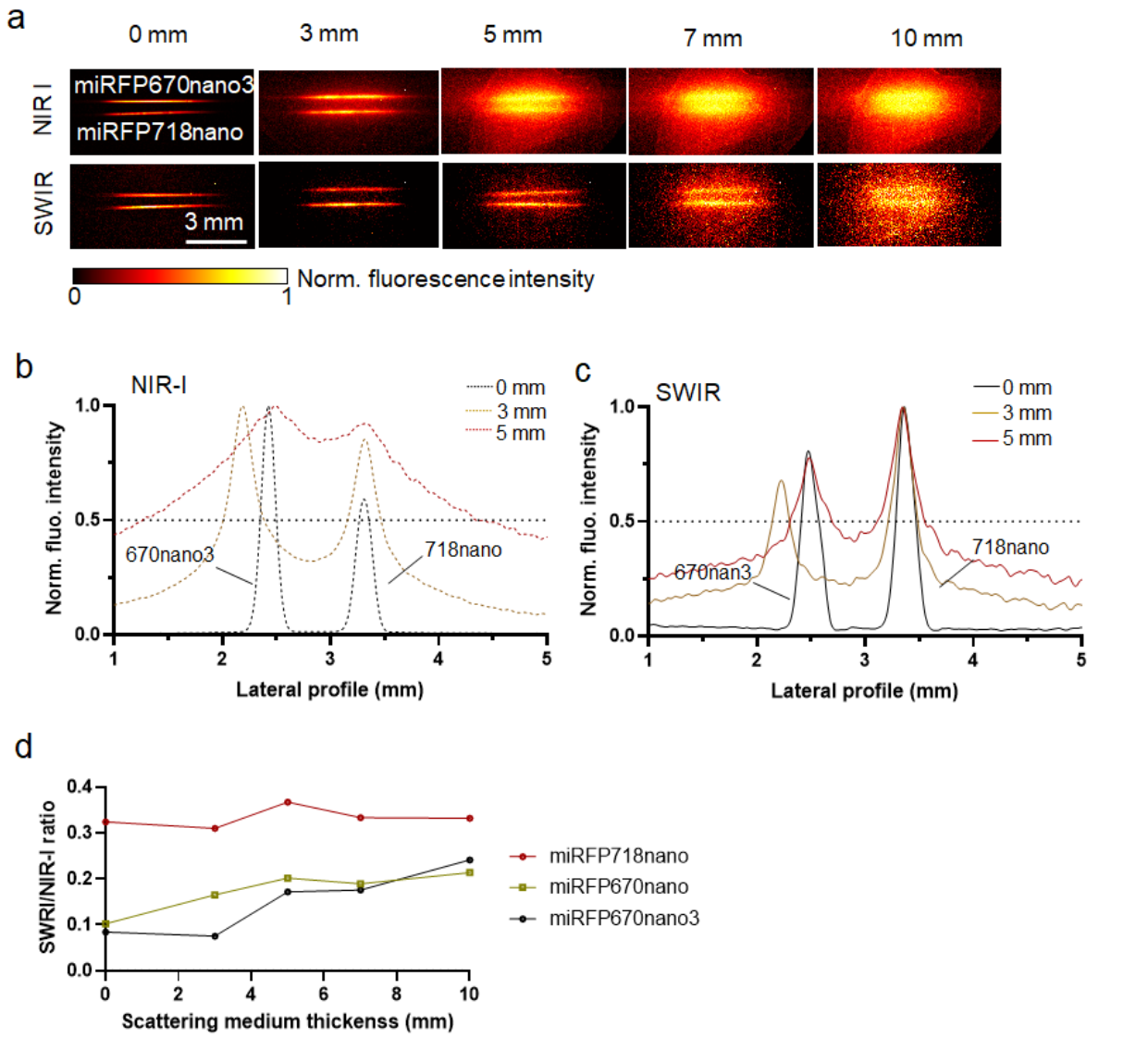

Supplementary Figure 13. Comparison of miRFP718nano- and miRFP670nano3-expressing mammalian cells in phantom. (**a**) The NIR-I and SWIR images of a pair of 100-μm diameter tubes filled with miRFP670nano3- or miRFP718nano-expressing HEK293T cells, overlayed by optically scattering medium at depths up to 10 mm. (**b**) The NIR-I signal profiles across the pair of tubes at depth of 0 mm, 3 mm and 5 mm. (**c**) The corresponding SWIR signal profiles at depth of 0 mm, 3 mm, and 5 mm. (**d**) The ratio of the SWIR/NIR-I emission by the miRFP718nano-, miRFP670nano-, and miRFP670nano3-expressing HEK293T cells at different depths in scattering medium.

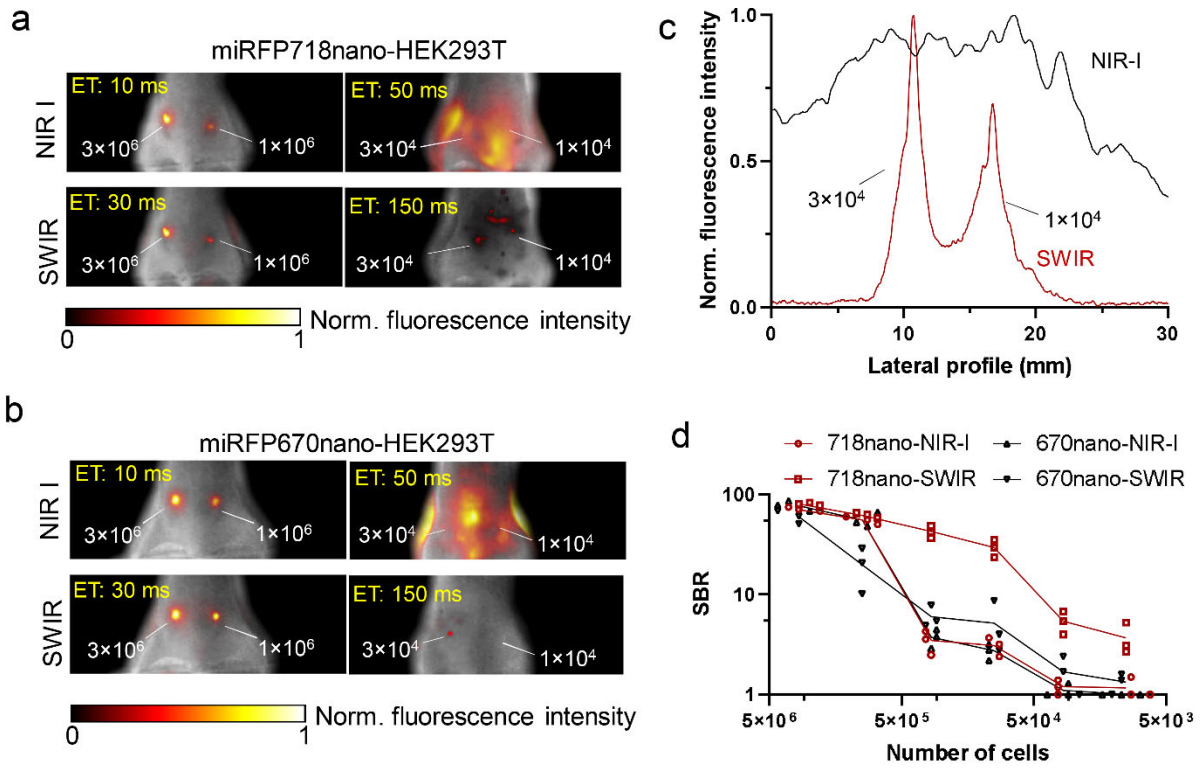

Supplementary Figure 14. NIR-I and SWIR imaging of mammalian cells in living mice. (**a**) Representative NIR-I and SWIR images of miRFP718nano-expressing HEK293T cells injected in the mouse mammary fat pad with different cell numbers. (**b**) Representative NIR-I and SWIR images of miRFP670nano-expressing HEK293Tcells injected into the mouse mammary fat pad with different cell numbers. (**c**) The NIR-I and SWIR signal profiles with miRFP718nano-expressing HEK293T cell number of 3×10^4 and 1×10^4, respectively. (**d**) The signal-to-background ratio (SBR) of the NIR-I and SWIR images with different cell numbers in the mammary glands (n = 3). No thresholding was applied in the imaging processing. The seemingly smaller fluorescence region with longer exposure time was due to much weaker background autofluorescence in the SWIR emission window.

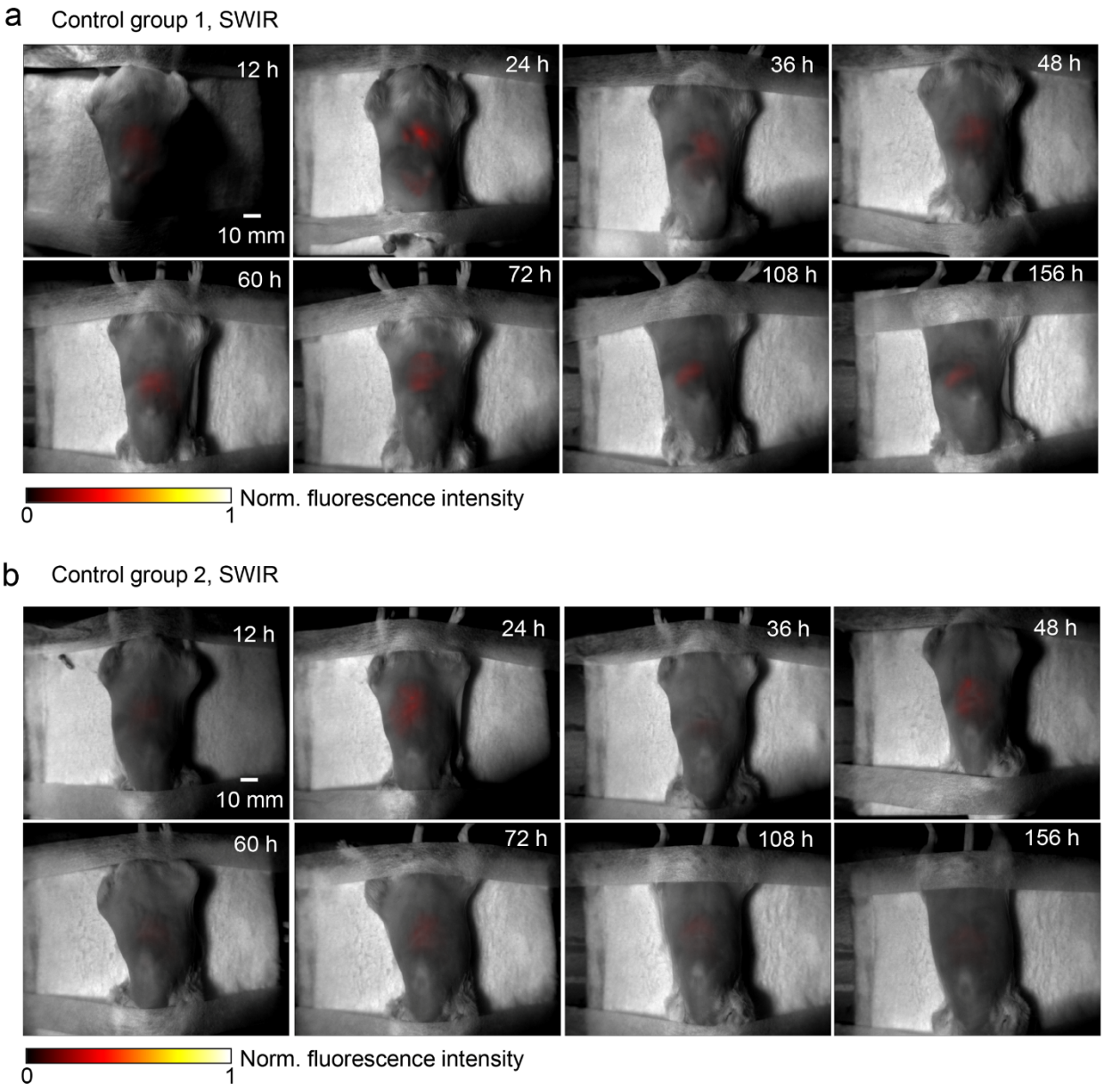

Supplementary Figure 15. SWIR imaging of the two control groups used in the NF-κB experiments. (a) Representative SWIR images of the first control group at different time points. This group received NF-κB-based miRFP718nano reporter plasmid through the tail vein, but no LPS injection after 72 h (n =3). **(b)** Representative SWIR images of the second control group at different time points. This group received PBS injection through the tail vein, and then i.p. injection of PBS after 72 h (n =3).

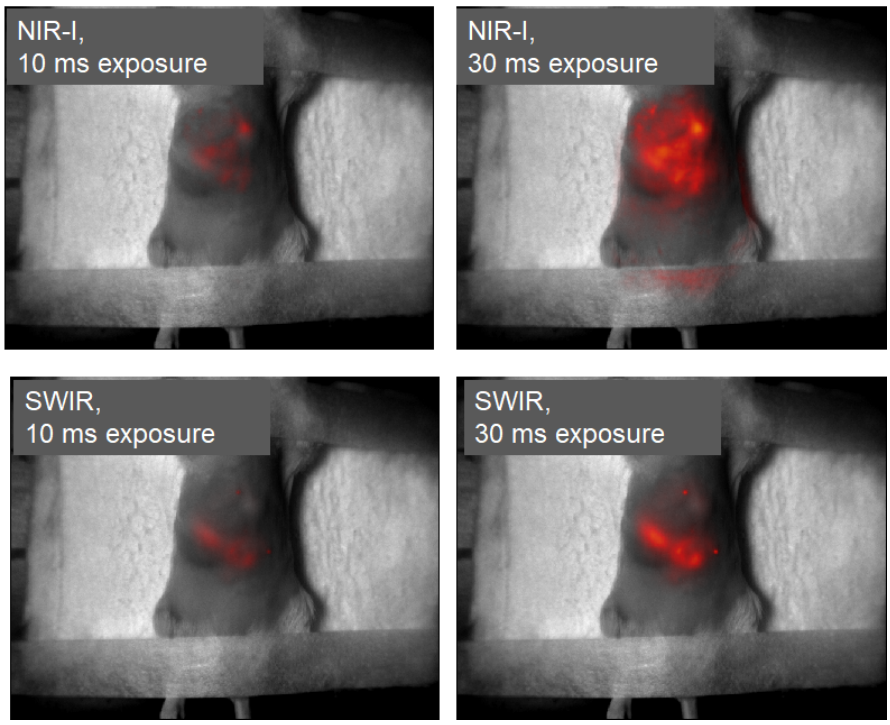

Supplementary Figure 16. Comparison of longer exposure times on SWIR and NIR-I imaging. NIR-I and SWIR images of the mouse 72 h after receiving miRFP718nano-based reporter of inflammation, with different exposure times of 10 ms and 30 ms. While a longer exposure time degraded the NIR-I image contrast due to the autofluorescence signals, the SWIR image has shown improved image contrast.

Supplementary Table 1. Properties of monomeric NIR FPs designed from various bacterial photoreceptors.

NIR FP	Ex, nm	Em, nm	Relative emission above 1000 nm[a]	Extinction coefficient, $M^{-1}cm^{-1}$	Quantum yield (QY), %	Relative emission above 1000 nm multiplied by QY	Molecular brightness *vs.* miRFP670nano, %	p*K*a$_1$ (acid)	p*K*a$_2$ (alkali)	Photostability in HeLa cells, $t_{1/2}$, s	Brightness in mammalian cells *vs.* miRFP670nano, % [b]	Ref.
miRFP670nano	645	670	0.3	95,000	10.8	3.3	100	3.7	8.0	545	100	[1]
miRFP718nano	690	718	1	79,000	5.6	5.6	43	3.8	10.5	1254	55	this work
miRFP670nano3	645	670	0.29	129,000	18.5	5.4	233	4.2	11	675	412	
miRFP703	674	703	0.53	90,900	8.6	4.6	76	4.5	>9.5	394	61	[3]
miRFP709	683	709	0.65	78,400	5.4	3.5	41	4.5	9.2	192	42	
SNIFP	697	720	n.d.	75,000 [c]	2.2	n.d.	16	4.5	>9.0	n.a.	n.a.	[4]
mIFP	683	704	n.d.	82,000	8.4	n.d.	67	4.5	9.2	54	26	[5, 6]
BDFP1.5	688	711	n.d.	74,000	5.0	n.d.	36	2.0	>10	1310 [c]	0.5 [d]	[7]

[a]Determined as integrated emission spectrum above 1000 nm normalized to the total integrated emission spectrum.

[b]Unless otherwise stated, it is determined as effective NIR fluorescence in live HeLa cells 72 h after transfection with no supply of exogenous BV and after normalization to the fluorescence of co-transfected EGFP.

[c]Estimated from SNIFP absorption spectrum in Supplementary Figure 2a in the original paper[4].

[d]Based on the comparison with smURFP in HEK293 cells in[7].

n.d., not determined..

Supplementary Table 2. Data collection statistics for miRFP718nano crystal.

Space group	*C*2
Unit cell parameters (Å, º)	a = 122.2
	b = 103.2
	c = 75.6
	β = 125.8
Temperature (K)	100
Wavelength (Å)	1.00
Resolution (Å)	30.0 – 1.7
Total reflections	285,750
Unique reflections	80,892
Completeness (%)	96.6 (96.4)
I/σ<I>	18.7 (1.6)
R-merge	0.047 (0.63)
Multiplicity	3.5 (3.4)

Data in parentheses are given for the outermost resolution shell 1.76 – 1.7 Å

Supplementary Table 3. Refinement statistics for miRFP718nano crystal.

No. of protein atoms	5,190
No. of solvent atoms	778
Resolution range (Å)	30.0 – 1.7
R-work	0.157
R-free	0.196
R.m.s.d. bond lengths (Å)	0.013
R.m.s.d. angles (º)	2.39
R.m.s.d. chirality (º)	0.089
R.m.s.d. planarity (º)	0.015
R.m.s.d. dihedral (º)	19.2
Mean B factors (Å^2)	
Protein atoms	
overall	27.7
main chain	25.3
side chain	30.1
chromophore	23.9
Water	43.1
Ramachandran statistics (%)	
(for non-Gly/Pro residues)	
most favorable	94.7
additional allowed	5.0
generously allowed	0.3

Supplementary Table 4. Sequences of oligonucleotides.

Oligonucleotide	Sequence (5'-3')
pBAD For	ATGCCATAGCATTTTTATCC
pBAD Rev	GATTTAATCTGTATCAGG
CMV For	AAATGGGCGGTAGGCGTGTAC
pcDNA Rev	TAGAAGGCACAGTCGAGGC
miRFPnano-KpnI For	AAAGGTACCATGGCAAACCTGGACAAG
miRFPnano-EcoRI Rev	AAAGAATTCAGCTAGCTCTGCTGGATGGCGATGC
miRFPnano-N-terminal fusions For	AAACCGGTAATGGCAAACCTGGACAAG
miRFPnano-N-terminal fusions Rev	ATAGGTACCGTACTCGTCCTGGTCTTC
miRFPnano-C-terminal fusions For	AAGCTAGCGGTACCATGGCAAACC
miRFPnano-C-terminal fusions Rev	TTAGATCTTCCTCCTGATCCACCACCTCCAGAACCACCTCCTCCTGATC CACCACCTCCGCTCTGCTGGATGGCGATGCCC
miRFPnano-actin For	TATAGATCTATGGATGATGATATCGCCGCG
miRFPnano-actin Rev	ATATCTAGACTAGAAGCATTTGCGGTGG
miRFPnano-linker-BamHI For	AAGGATCCGGTGGGGGAGGCAGCATGGCAAACCTGGACAAGATGC
miRFPnano-linker-AgeI Rev	TTACCGGTGCTCCCGCCACCTCCGCTCTGCTGGATGGCGATGC
C86XFor	CCGCAAACCTGACAGAGNNSTACAGGGATCTGCTGACACAG
C86Rev	CTCTGTCAGGTTTGCGGTG
V115L113For	GGGCAAGAAGCTGTGGGGCGGCTTGTTCGCACACCAGCTGGCGGCCC C
V115L113Rev	GGGGCCGCCAGCTGGTGTGCGAACAAGCCGCCCCACAGCTTCTTGCCC
V115S H117Ffor	GGGCAAGAAGCTGTGGGGCCTGTTGAGCGCATTCCAGCTGGCGGCCCC
V115S H117Frev	GGGGCCGCCAGCTGGAATGCGCTCAACAGGCCCCACAGCTTCTTGCCC
Rev R57C	GCCCCTTGTCTCCATGAAGTAGCAATCCCGCACCTGGGTCTTC
F R57c	GAAGACCCAGGTGCGGGATTGCTACTTCATGGAGACAAGGGGC
B2AR-AgeR	TTACCGGTGCTCCCGCCACCTCCAGCTCTGCTGGATGGCG
B2AR-BamF	AAGGATCCGGTGGGGGAGGCAGCATGGCAAACCTGGACAAG
mitoHind-F	AAAAGCTTATGTCCGTCCTGACGCCGC
mitoKpn-R	TTGGTACCACTCCCAGATCCGCCCCCCAACGAATGGATCTTG
NF-KpnFor	CCGGTACCTGAGCTCGCTAGC
NF-Rev	CTTGTCCAGGTTTGCCATGGTGGCTTTACCAACAGTAC
718-For	GTACTGTTGGTAAAGCCACCATGGCAAACCTGGACAAG
718stopEcoR	CAGAATTCAGCTAGCTCTGCTGGATGGCGATGC

References

1. Oliinyk, O.S., Shemetov, A.A., Pletnev, S., Shcherbakova, D.M. & Verkhusha, V.V. Smallest near-infrared fluorescent protein evolved from cyanobacteriochrome as versatile tag for spectral multiplexing. *Nat Commun* **10**, 279 (2019).
2. Baloban, M. et al. Designing brighter near-infrared fluorescent proteins: insights from structural and biochemical studies. *Chem Sci* **8**, 4546-4557 (2017).
3. Shcherbakova, D.M. et al. Bright monomeric near-infrared fluorescent proteins as tags and biosensors for multiscale imaging. *Nat Commun* **7**, 12405 (2016).
4. Kamper, M., Ta, H., Jensen, N.A., Hell, S.W. & Jakobs, S. Near-infrared STED nanoscopy with an engineered bacterial phytochrome. *Nat Commun* **9**, 4762 (2018).
5. Yu, D. et al. A naturally monomeric infrared fluorescent protein for protein labeling in vivo. *Nat Methods* **12**, 763-765 (2015).
6. Shemetov, A.A., Oliinyk, O.S. & Verkhusha, V.V. How to Increase Brightness of Near-Infrared Fluorescent Proteins in Mammalian Cells. *Cell Chem Biol* **24**, 758-766 e753 (2017).
7. Ding, W.L. et al. Small monomeric and highly stable near-infrared fluorescent markers derived from the thermophilic phycobiliprotein, ApcF2. *Biochim Biophys Acta* **1864**, 1877-1886 (2017).